



Contents lists available at ScienceDirect

## International Journal of Plasticity

journal homepage: [www.elsevier.com/locate/ijplas](http://www.elsevier.com/locate/ijplas)

# On stress-state dependent plasticity modeling: Significance of the hydrostatic stress, the third invariant of stress deviator and the non-associated flow rule

Xiaosheng Gao<sup>a,\*</sup>, Tingting Zhang<sup>a</sup>, Jun Zhou<sup>a</sup>, Stephen M. Graham<sup>b</sup>, Matthew Hayden<sup>c</sup>, Charles Roe<sup>c</sup>

<sup>a</sup> Department of Mechanical Engineering, The University of Akron, Akron, OH 44325, USA

<sup>b</sup> Department of Mechanical Engineering, United States Naval Academy, Annapolis, MD 21402, USA

<sup>c</sup> Alloy Development and Mechanics Branch, Naval Surface Warfare Center, West Bethesda, MD 20817, USA

## ARTICLE INFO

## Article history:

Received 19 February 2010

Received in final revised form 20 April 2010

Available online xxxx

## Keywords:

Plasticity modeling

Stress triaxiality

Lode angle

Modified Gurson model

Non-associated flow rule

## ABSTRACT

It has been shown that the plastic response of many materials, including some metallic alloys, depends on the stress state. In this paper, we describe a plasticity model for isotropic materials, which is a function of the hydrostatic stress as well as the second and third invariants of the stress deviator, and present its finite element implementation, including integration of the constitutive equations using the backward Euler method and formulation of the consistent tangent moduli. Special attention is paid for the adoption of the non-associated flow rule. As an application, this model is calibrated and verified for a 5083 aluminum alloy. Furthermore, the Gurson–Tvergaard–Needleman porous plasticity model, which is widely used to simulate the void growth process of ductile fracture, is extended to include the effects of hydrostatic stress and the third invariant of stress deviator on the matrix material.

© 2010 Elsevier Ltd. All rights reserved.

## 1. Introduction

Plasticity describes the deformation of a material undergoing non-reversible changes of shape in response to applied forces. Our ancestors in ancient times already recognized the plastic behavior of metals as they attempted to make various tools and weapons. However, the scientific study of plasticity may justly be regarded as beginning in 1864 when Tresca published his results on punching and extrusion experiments and formulated his famous yield criterion (Tresca, 1864). This yield criterion was then used by Saint-Venant (1870) and Levy (1870) in their development of a theory of rigid-perfectly plastic solid. Another well known yield criterion was proposed by von Mises (1913) on the basis of purely mathematical considerations and later was interpreted by Hencky (1924) as plastic yielding occurs when the elastic shear-strain energy reaches a critical value. Von Mises also independently proposed equations similar to Levy's for rigid-perfectly plastic materials. Other important contributions in the early development of the plasticity theory include the works by Prandtl (1925), Reuss (1930), among others. Subsequently, within the scope of elastic–plastic materials under small deformation, the notation of yield in the stress space formulation was generalized to cover work-hardening materials and a unified theory of plasticity began to emerge after World War II (Hill, 1950; Mendelson, 1968). The flow theory is the most widely known theory of plasticity, which consists of a yield criterion, a flow rule, a hardening law and the loading–unloading conditions. The yield criterion determines the stress-state when yielding occurs, the flow rule describes the increment of plastic strain after yielding,

\* Corresponding author. Tel.: +1 330 972 2415; fax: +1 330 972 6027.

E-mail address: [xgao@uakron.edu](mailto:xgao@uakron.edu) (X. Gao).

Report Documentation Page				Form Approved OMB No. 0704-0188	
Public reporting burden for the collection of information is estimated to average 1 hour per response, including the time for reviewing instructions, searching existing data sources, gathering and maintaining the data needed, and completing and reviewing the collection of information. Send comments regarding this burden estimate or any other aspect of this collection of information, including suggestions for reducing this burden, to Washington Headquarters Services, Directorate for Information Operations and Reports, 1215 Jefferson Davis Highway, Suite 1204, Arlington VA 22202-4302. Respondents should be aware that notwithstanding any other provision of law, no person shall be subject to a penalty for failing to comply with a collection of information if it does not display a currently valid OMB control number.					
1. REPORT DATE <b>20 APR 2010</b>		2. REPORT TYPE		3. DATES COVERED <b>00-00-2010 to 00-00-2010</b>	
4. TITLE AND SUBTITLE <b>On stress-state dependent plasticity modeling: Significance of the hydrostatic stress, the third invariant of stress deviator and the non-associated flow rule</b>				5a. CONTRACT NUMBER	
				5b. GRANT NUMBER	
				5c. PROGRAM ELEMENT NUMBER	
6. AUTHOR(S)				5d. PROJECT NUMBER	
				5e. TASK NUMBER	
				5f. WORK UNIT NUMBER	
7. PERFORMING ORGANIZATION NAME(S) AND ADDRESS(ES) <b>United States Naval Academy, Department of Mechanical Engineering, Annapolis, MD, 21402</b>				8. PERFORMING ORGANIZATION REPORT NUMBER	
9. SPONSORING/MONITORING AGENCY NAME(S) AND ADDRESS(ES)				10. SPONSOR/MONITOR'S ACRONYM(S)	
				11. SPONSOR/MONITOR'S REPORT NUMBER(S)	
12. DISTRIBUTION/AVAILABILITY STATEMENT <b>Approved for public release; distribution unlimited</b>					
13. SUPPLEMENTARY NOTES					
14. ABSTRACT <b>see report</b>					
15. SUBJECT TERMS					
16. SECURITY CLASSIFICATION OF:			17. LIMITATION OF ABSTRACT <b>Same as Report (SAR)</b>	18. NUMBER OF PAGES <b>15</b>	19a. NAME OF RESPONSIBLE PERSON
a. REPORT <b>unclassified</b>	b. ABSTRACT <b>unclassified</b>	c. THIS PAGE <b>unclassified</b>			

the hardening law characterizes the evolution of the flow stress with increased plastic deformation, and the loading–unloading conditions specify if the stress path moves outward from the current yield surface, inward from the current surface or along the current surface.

The most popular continuum plasticity model is the so-called  $J_2$ -flow theory. This theory assumes hydrostatic stress as well as the third invariant of the stress deviator has no effect on plastic yielding and the flow stress and has been widely employed to describe the plastic response of metals. However, increasing experimental evidences show that this assumption is invalid for many materials. Inspired by the extensive experimental results reported by Spitzig et al. (1975, 1976) on the behavior of high-strength metals undergoing uniaxial tension and compression, Brunig (1999) presented an  $I_1$ – $J_2$  yield criterion, which is similar to the Drucker–Prager yield condition in soil mechanics (Drucker and Prager, 1952), to describe the effect of the hydrostatic stress on the plastic flow properties of metals. Later, the  $I_1$ – $J_2$  plasticity model was applied by Brunig et al. (2008) to study the effect of stress triaxiality on the onset and evolution of damage in ductile metals. In Brunig et al. (2000), the authors added a  $J_3$  term in the yield function to study the deformation and localization behavior of hydrostatic stress sensitive metals. Kuroda (2004) presented a phenomenological plasticity model accounting for hydrostatic stress-sensitivity and vertex-type of effect. Hu and Wang (2005) proposed a stress-state dependent yield criterion for isotropic ductile materials. Cazacu and Barlat (2003) and Soare et al. (2007) extended Drucker's  $J_2$ – $J_3$  yield function (Drucker, 1949) to include plastic anisotropy and applied it to simulate sheet forming. Plunkett et al. (2008) and Cazacu et al. (2010) extended the isotropic yield function proposed by Cazacu et al. (2006) to account for the anisotropic plastic response of textured metals. Bai and Wierzbicki (2008) discussed a pressure and Lode dependent metal plasticity model and its application in failure analysis. Gao et al. (2009) noticed the plastic response of a 5083 aluminum alloy is stress-state dependent and were forced to use different stress–strain curves to analyze specimens experiencing different stress states. In a most recent study, Mirone and Corallo (2010) found that, for the metals they tested, the hydrostatic stress plays a significant role in accelerating failure but has negligible effect on the stress–plastic strain relationship, while the Lode angle has a considerable effect in modifying the stress–strain curves but does not significantly affect the failure strains. These findings agree with the findings by Gao et al. (2009).

A common approach in the metal plasticity theory is the adoption of the so-called associated flow rule or normality condition, requiring the yield function and the flow potential to be identical. Although the normality condition is a consequence of the postulate of maximum plastic dissipation, many studies, such as Mroz (1963), Nemat-Nasser and Shokooh (1980), Nemat-Nasser (1983, 1992), Runesson and Mroz (1989), Brunig et al. (2000), Stoughton (2002) and Stoughton and Yoon (2004, 2006), indicate that appropriate constitutive description of many materials can be achieved by using the less restrictive non-associated flow rule. Brunig (1999) and Brunig et al. (2000) demonstrated that pressure sensitive yielding and non-associated flow rule remarkably influence the onset of localization and the subsequent localization behavior. To model the ductile fracture process in solids, Ma and Kishimoto (1998) proposed a non-associated flow rule to characterize the yield and plastic deformation of void-containing materials, where the yield function takes the form of the Gurson–Tvergaard–Needleman porous plasticity model (Gurson, 1977; Tvergaard, 1981, 1982; Tvergaard and Needleman, 1984) while the flow potential takes a slightly different form. In a recent publication, Cvitanic et al. (2008) presented detailed finite element formulations for sheet metal forming based on non-associated plasticity.

In this paper, we describe a plasticity model for isotropic materials, which is dependent on the second and third invariants of the stress deviator as well as the hydrostatic stress, and present its finite element implementation including integration of the constitutive equations using the backward Euler method and the formulation of the consistent tangent moduli. The derivation will be based on small-strain formulation. For finite strain plasticity, kinematic transformations are performed first so that the constitutive equations governing finite deformation are formulated using strains–stresses and their rates defined on an unrotated frame of reference. Once the kinematic transformations have eliminated rotation effects on rates of the tensorial quantities, the stress updating procedure and the consistent tangent stiffness formulation remain the same as those for small-strain formulation. Most commercial finite element programs adopt this kind of treatment for finite strain plasticity thus only small-strain formulation needs to be considered in development of a user material subroutine. As an application, the proposed plasticity model is calibrated and verified for a 5083 aluminum alloy. Furthermore, we extend the Gurson–Tvergaard–Needleman porous plasticity model to include the effects of the stress state and present a few numerical examples. The modified porous plasticity model is expected to improve accuracy in predicting ductile fracture process of certain materials.

## 2. Plasticity modeling

### 2.1. Influence of $I_1$ and $J_3$

Let  $\sigma_{ij}$  be the stress tensor and  $\sigma_1$ ,  $\sigma_2$  and  $\sigma_3$  be the principal stress values. The hydrostatic stress (or mean stress) can be expressed as

$$\sigma_h = \frac{1}{3}I_1 = \frac{1}{3}\sigma_{ii} = \frac{1}{3}(\sigma_1 + \sigma_2 + \sigma_3) \quad (1)$$

where  $I_1$  represents the first invariant of the stress tensor and the summation convention is adopted for repeated indices. Let  $\sigma'_{ij}$  be the stress deviator tensor and  $\sigma'_1, \sigma'_2$  and  $\sigma'_3$  be its principal values, i.e.,

$$\sigma'_{ij} = \sigma_{ij} - \sigma_h \delta_{ij} \quad (2)$$

where  $\delta_{ij}$  represents the Kronecker delta. It is obvious that the first invariant of the stress deviator tensor is zero. The second and third invariants of the stress deviator tensor are defined as

$$J_2 = \frac{1}{2} \sigma'_{ij} \sigma'_{ji} = -(\sigma'_1 \sigma'_2 + \sigma'_2 \sigma'_3 + \sigma'_3 \sigma'_1) = \frac{1}{6} [(\sigma_1 - \sigma_2)^2 + (\sigma_2 - \sigma_3)^2 + (\sigma_3 - \sigma_1)^2] \quad (3)$$

$$J_3 = \det(\sigma'_{ij}) = \frac{1}{3} \sigma'_{ij} \sigma'_{jk} \sigma'_{ki} = \sigma'_1 \sigma'_2 \sigma'_3$$

For isotropic materials, the plastic behavior is often described by the stress invariants  $I_1, J_2$  and  $J_3$  and consequently, the general forms of the yield function ( $F$ ) and the flow potential ( $G$ ) are expressed as functions of  $I_1, J_2$  and  $J_3$ . Eq. (4) describes the yield condition

$$F(I_1, J_2, J_3) - \bar{\sigma} = 0 \quad (4)$$

where  $\bar{\sigma}$  is the hardening parameter. When material deforms plastically, the inelastic part of the deformation is defined by the flow rule

$$\dot{\epsilon}^p_{ij} = \dot{\lambda} \frac{\partial G(I_1, J_2, J_3)}{\partial \sigma_{ij}} \quad (5)$$

where  $\dot{\epsilon}^p_{ij}$  are the rates of the plastic strain components and  $\dot{\lambda}$  is a positive scalar called the plastic multiplier.

A simple form of the yield function is given as follows

$$F = c_1 \left( a_1 I_1^6 + 27 J_2^3 + b_1 J_3^2 \right)^{1/6} \quad (6)$$

where  $a_1, b_1$  and  $c_1$  are material constants. The yield function defined by Eq. (6) is a first order homogeneous function of stress, from which an equivalent stress can be defined as

$$\sigma_e = F \quad (7)$$

The constant  $c_1$  can be found by substituting the uniaxial condition into Eq. (6), thus

$$c_1 = \left( a_1 + \frac{4}{729} b_1 + 1 \right)^{-1/6} \quad (8)$$

When the material is subjected to a uniaxial stress  $\sigma$ , the value of  $c_1$  given by Eq. (8) ensures  $\sigma_e = \sigma$ .

The flow potential takes a similar form, i.e.,

$$G = c_2 \left( a_2 I_1^6 + 27 J_2^3 + b_2 J_3^2 \right)^{1/6} \quad (9)$$

where  $c_2 = (a_2 + 4b_2/729 + 1)^{-1/6}$ .

If the flow potential and the yield function are identical, i.e.,  $F = G$ , Eq. (5) becomes the so-called associated flow rule. Furthermore, if  $a_1 = b_1 = a_2 = b_2 = 0$ , the plasticity model degenerates to the formulation of classical  $J_2$ -flow theory and  $\sigma_e$  defined by Eq. (7) becomes the von Mises equivalent stress.

The hardening parameter depends on the strain history. By enforcing the equivalence of plastic work, i.e.,

$$\bar{\sigma} \dot{\bar{\epsilon}}^p = \sigma_{ij} \dot{\epsilon}^p_{ij} \quad (10)$$

the equivalent plastic strain increment can be defined as

$$\dot{\bar{\epsilon}}^p = \sigma_{ij} \dot{\epsilon}^p_{ij} / \bar{\sigma} \quad (11)$$

Therefore, the hardening behavior can be described by a stress vs. plastic strain relation  $\bar{\sigma}(\bar{\epsilon}^p)$ , where  $\bar{\epsilon}^p = \int \dot{\bar{\epsilon}}^p dt$ .

Since the flow potential is taken to be a first order homogeneous function of stress, Euler's homogeneous function theorem results in

$$\sigma_{ij} \dot{\epsilon}^p_{ij} = \dot{\lambda} \sigma_{ij} \frac{\partial G}{\partial \sigma_{ij}} = \dot{\lambda} G \quad (12)$$

From (10) and (12), the plastic multiplier and the equivalent plastic strain rate can be related through

$$\dot{\lambda} = \dot{\bar{\epsilon}}^p \frac{\bar{\sigma}}{G} = \dot{\bar{\epsilon}}^p \frac{F}{G} \quad (13)$$

If the material follows the associated flow rule,  $F = G$  and  $\dot{\lambda} = \dot{\bar{\epsilon}}^p$ .

Because of the  $I_1$  term in the flow potential  $G$ , the plastic response becomes dilatant, with the rate of volume change given by

$$\dot{\epsilon}_{kk}^p = \dot{\lambda} \frac{\partial G}{\partial \sigma_{kk}} = \dot{\lambda} \left( 3c_2^6 a_2 I_1^5 / G^5 \right) = 3c_2^6 a_2 I_1^5 \dot{\epsilon}^p \frac{F}{G^6} \quad (14)$$

## 2.2. Numerical implementation of the $I_1$ – $J_2$ – $J_3$ plasticity model

Following the procedures of Aravas (1987) and Kim and Gao (2005), we implement the  $I_1$ – $J_2$ – $J_3$  plasticity model outlined in the previous section into ABAQUS (SIMULIA, 2008) via a user defined subroutine.

### 2.2.1. Stress update

We adopt the backward Euler method to integrate the rate constitutive equations. For the strain driven integration algorithm, the stresses and state variables are known at the start of each increment and their values need to be updated at the end of the increment corresponding to the total strain increment. The elasticity equations give

$$(\sigma_{ij})^{t+\Delta t} = C_{ijkl}^e (\epsilon_{kl})^{t+\Delta t} = C_{ijkl}^e \left\{ (\epsilon_{kl})^t + \Delta \epsilon_{kl} - \Delta \epsilon_{kl}^p \right\} = \sigma_{ij}^T - C_{ijkl}^e \Delta \epsilon_{kl}^p \quad (15)$$

where

$$\sigma_{ij}^T = C_{ijkl}^e \left\{ (\epsilon_{kl})^t + \Delta \epsilon_{kl} \right\} \quad (16)$$

is the elastic predictor,  $t$  represents the time at the start of the increment,  $t + \Delta t$  represents the time at the end of the increment, and the superscripts  $e$  and  $p$  denote elastic and plastic components, respectively. The total strain increment  $\Delta \epsilon_{kl}$  is known, and if the linear elastic behavior is isotropic, the elastic moduli  $C_{ijkl}^e$  can be expressed as

$$C_{ijkl}^e = G(\delta_{ik}\delta_{jl} + \delta_{il}\delta_{jk}) + \left( K - \frac{2}{3}G \right) \delta_{ij}\delta_{kl} \quad (17)$$

where  $G$  and  $K$  are the elastic shear and bulk moduli, respectively. Therefore, to update stresses, the plastic strain increments need to be determined. The following outlines the procedure for computing  $\Delta \epsilon_{ij}^p$ .

The yield condition and the flow rule are written as

$$F(I_1^{t+\Delta t}, J_2^{t+\Delta t}, J_3^{t+\Delta t}) - \bar{\sigma}(\bar{\epsilon}_{t+\Delta t}^p) = 0 \quad (18)$$

and

$$\Delta \epsilon_{ij}^p = \Delta \lambda \left( \frac{\partial G(I_1, J_2, J_3)}{\partial \sigma_{ij}} \right)^{t+\Delta t} \quad (19)$$

Eqs. (18) and (19), when considered together with Eq. (15), result in 10 equations for  $\Delta \lambda$  and nine components of  $\Delta \epsilon_{ij}^p$ , among which seven equations are independent due to the symmetry of  $\Delta \epsilon_{ij}^p$ . If the state variable  $\bar{\epsilon}^p$  is updated and thus  $\bar{\sigma}(\bar{\epsilon}_{t+\Delta t}^p)$  is known, these equations can be solved iteratively for  $\Delta \epsilon_{ij}^p$  and  $\Delta \lambda$  using the Newton–Raphson method. The iterative process follows these steps: (1) assume  $\Delta \epsilon_{ij}^p = 0$  and use Eq. (15) to estimate  $\sigma_{ij}^{t+\Delta t}$ ; (2) use Eqs. (18) and (19) to solve for  $\Delta \epsilon_{ij}^p$ ; (3) update stresses using Eq. (15); (4) repeat steps (2)–(3) until convergence conditions are satisfied.

To update  $\bar{\epsilon}^p$ , consider the hardening law and the evolution equation for  $\bar{\epsilon}^p$

$$\bar{\sigma} = \bar{\sigma}(\bar{\epsilon}_{t+\Delta t}^p) = \bar{\sigma}(\bar{\epsilon}_t^p + \Delta \bar{\epsilon}^p) \quad (20)$$

and

$$\bar{\sigma} \Delta \bar{\epsilon}^p = \sigma_{ij}^{t+\Delta t} \Delta \epsilon_{ij}^p \quad (21)$$

At each iteration of  $\Delta \epsilon_{ij}^p$ ,  $\Delta \bar{\epsilon}^p$  and  $\bar{\sigma}(\bar{\epsilon}_{t+\Delta t}^p)$  can be obtained by solving Eqs. (20) and (21) iteratively using the Newton–Raphson method.

### 2.2.2. The consistent tangent moduli

Simo and Taylor (1985) showed that use of the consistent tangent moduli significantly improves the convergence characteristics of the overall equilibrium iterations. The consistent tangent stiffness corresponding to the backward Euler integration can be obtained by linearization of Eq. (15).

$$J_{ijkl} = \left( \frac{\partial \sigma_{ij}}{\partial \epsilon_{kl}} \right)^{t+\Delta t} \quad (22)$$

Since all quantities in calculating  $J_{ijkl}$  are referred to time  $t + \Delta t$ , the superscript  $t + \Delta t$  will be dropped from hereafter. Eq. (15) can be rewritten as

$$\sigma_{ij} = C_{ijkl}^e \epsilon_{kl}^e = C_{ijkl}^e (\epsilon_{kl} - \epsilon_{kl}^p) = C_{ijkl}^e \left\{ \epsilon_{kl} - (\epsilon_{kl}^p)^t - \Delta \epsilon_{kl}^p \right\} \quad (23)$$

Differentiating (23) results in

$$\partial \sigma_{ij} = C_{ijkl}^e \partial \epsilon_{kl} - C_{ijkl}^e \partial (\Delta \epsilon_{kl}^p) \quad (24)$$

The relationship between  $\partial \sigma_{ij}$  and  $\partial (\Delta \epsilon_{kl}^p)$  can be found as follows.

Let  $h$  be the hardening modulus, i.e.,  $h = \Delta \bar{\sigma} / \Delta \bar{\epsilon}^p$ , then Eq. (21) can be rewritten as

$$\Delta \bar{\sigma} = \frac{h \sigma_{ij} \Delta \epsilon_{ij}^p}{\bar{\sigma}} \quad (25)$$

By differentiating (25) and simplifying the resulted relation, the following equation can be obtained

$$\partial \bar{\sigma} = \frac{h \bar{\sigma} \Delta \epsilon_{ij}^p}{\bar{\sigma}^2 + h \sigma_{mn} \Delta \epsilon_{mn}^p} \partial \sigma_{ij} + \frac{h \bar{\sigma} \sigma_{ij}}{\bar{\sigma}^2 + h \sigma_{mn} \Delta \epsilon_{mn}^p} \partial (\Delta \epsilon_{ij}^p) \quad (26)$$

Differentiating Eq. (18) and combining the result with Eq. (26) give

$$\frac{h \bar{\sigma} \sigma_{ij}}{\bar{\sigma}^2 + h \sigma_{mn} \Delta \epsilon_{mn}^p} \partial (\Delta \epsilon_{ij}^p) = \left( \frac{\partial F(I_1, J_2, J_3)}{\partial \sigma_{ij}} - \frac{h \bar{\sigma} \Delta \epsilon_{ij}^p}{\bar{\sigma}^2 + h \sigma_{mn} \Delta \epsilon_{mn}^p} \right) \partial \sigma_{ij} \quad (27)$$

Eliminating  $\Delta \lambda$  from the nine equations given by (19) results in eight equations, such as

$$\begin{aligned} \left( \frac{\partial G(I_1, J_2, J_3)}{\partial \sigma_{22}} \right) \Delta \epsilon_{11}^p - \left( \frac{\partial G(I_1, J_2, J_3)}{\partial \sigma_{11}} \right) \Delta \epsilon_{22}^p &= 0 \\ \left( \frac{\partial G(I_1, J_2, J_3)}{\partial \sigma_{22}} \right) \Delta \epsilon_{21}^p - \left( \frac{\partial G(I_1, J_2, J_3)}{\partial \sigma_{21}} \right) \Delta \epsilon_{22}^p &= 0 \\ &\vdots \end{aligned} \quad (28)$$

Differentiating (28) leads to

$$\begin{aligned} \left( \frac{\partial G}{\partial \sigma_{22}} \right) \partial (\Delta \epsilon_{11}^p) - \left( \frac{\partial G}{\partial \sigma_{11}} \right) \partial (\Delta \epsilon_{22}^p) &= \left( \Delta \epsilon_{22}^p \frac{\partial^2 G}{\partial \sigma_{11} \partial \sigma_{ij}} - \Delta \epsilon_{11}^p \frac{\partial^2 G}{\partial \sigma_{22} \partial \sigma_{ij}} \right) \partial \sigma_{ij} \\ \left( \frac{\partial G}{\partial \sigma_{22}} \right) \partial (\Delta \epsilon_{21}^p) - \left( \frac{\partial G}{\partial \sigma_{21}} \right) \partial (\Delta \epsilon_{22}^p) &= \left( \Delta \epsilon_{22}^p \frac{\partial^2 G}{\partial \sigma_{21} \partial \sigma_{ij}} - \Delta \epsilon_{21}^p \frac{\partial^2 G}{\partial \sigma_{22} \partial \sigma_{ij}} \right) \partial \sigma_{ij} \\ &\vdots \end{aligned} \quad (29)$$

Eqs. (27) and (29) provide nine equations between  $\partial (\Delta \epsilon_{ij}^p)$  and  $\partial \sigma_{ij}$ , which can be summarized as

$$\mathbf{K} \partial (\Delta \epsilon^p) = \mathbf{D} \partial \sigma \quad (30)$$

where  $\Delta \epsilon^p = \{\Delta \epsilon_{11}^p, \Delta \epsilon_{21}^p, \Delta \epsilon_{31}^p, \dots, \Delta \epsilon_{33}^p\}^T$ ,  $\sigma = \{\sigma_{11}, \sigma_{21}, \sigma_{31}, \dots, \sigma_{33}\}^T$ ,  $\mathbf{K}$  is the coefficient matrix of  $\partial (\Delta \epsilon^p)$  and  $\mathbf{D}$  is the coefficient matrix of  $\partial \sigma$ .

From Eqs. (24) and (30) we can obtain

$$\partial (\Delta \epsilon^p) = (\mathbf{K} + \mathbf{D} \mathbf{C}^e)^{-1} \mathbf{D} \mathbf{C}^e (\partial \epsilon) \quad (31)$$

where  $\mathbf{C}^e$  is a  $9 \times 9$  matrix representing the elasticity tensor  $C_{ijkl}^e$ . Finally, the consistent tangent matrix can be obtained by substituting (31) into (24)

$$\mathbf{J} = \partial \sigma / \partial \epsilon = \mathbf{C}^e - \mathbf{C}^e (\mathbf{K} + \mathbf{D} \mathbf{C}^e)^{-1} \mathbf{D} \mathbf{C}^e \quad (32)$$

### 2.3. A modified Gurson–Tvergaard–Needleman model

Ductile fracture of many structural materials is a result of void nucleation, growth and coalescence. The constitutive description of this mechanism has received a great deal of attention in the past 30 years, which leads to various forms of porous material models being developed to describe void growth and the associated macroscopic softening. One of the most famous porous plasticity models was due to Gurson (1977) with modifications by Tvergaard and Needleman (Tvergaard, 1981, 1982; Tvergaard and Needleman, 1984). In the Gurson–Tvergaard–Needleman model, an extra internal variable, the void volume fraction ( $f$ ), is introduced to capture the growth of cavities and its effect on material behavior. It is important to notice that the Gurson–Tvergaard–Needleman model reduces to that for  $J_2$ -flow theory of plasticity with isotropic hardening in the absence of voids ( $f = 0$ ).

Within the framework of the  $I_1$ – $J_2$ – $J_3$  plasticity theory outlined in Section 2.1, the yield function and flow potential of the Gurson–Tvergaard–Needleman model can be modified as

$$\Phi = \left(\frac{F}{\bar{\sigma}}\right)^2 + 2q_1 f \cosh\left(\frac{q_2 I_1}{2\bar{\sigma}}\right) - 1 - q_1^2 f^2 = 0 \quad (33)$$

and

$$\Psi = \left(\frac{G}{\bar{\sigma}}\right)^2 + 2q_1 f \cosh\left(\frac{q_2 I_1}{2\bar{\sigma}}\right) - 1 - q_1^2 f^2 = 0 \quad (34)$$

where  $F$  and  $G$  take the forms of Eqs. (6) and (9), i.e.,  $F = c_1 \left(a_1 I_1^6 + 27J_2^3 + b_1 J_3^2\right)^{1/6}$  and  $G = c_2 \left(a_2 I_1^6 + 27J_2^3 + b_2 J_3^2\right)^{1/6}$ ,  $I_1$ ,  $J_2$  and  $J_3$  are invariants of the macroscopic stress,  $f$  is the current void volume fraction,  $\bar{\sigma}$  is the current yield stress of the matrix material, and  $q_1$  and  $q_2$  are parameters introduced by Tvergaard (1981, 1982) to account for void interaction and matrix strain hardening. If  $a_1 = b_1 = a_2 = b_2 = 0$ , Eqs. (33) and (34) degenerate to the original Gurson–Tvergaard–Needleman model.

Porous material models contain an additional state variable,  $f$ . For the modified Gurson–Tvergaard–Needleman model, the evolution equation for  $f$  can be obtained by considering the rate of the net volume change

$$\dot{f} = (1 - f) \left[ \dot{\epsilon}_{kk}^p - 3c_2 a_2 I_1^5 \frac{F}{G^6} \right] \quad (35)$$

By enforcing equality between the rates of macroscopic plastic work and the matrix plastic dissipation, the matrix yield stress,  $\bar{\sigma}$ , and the matrix plastic strain rate,  $\dot{\epsilon}^p$ , are coupled through

$$(1 - f) \bar{\sigma} \dot{\epsilon}^p = \sigma_{ij} \dot{\epsilon}_{ij}^p \quad (36)$$

where the matrix material follows a prescribed hardening function  $\bar{\sigma}(\bar{\epsilon}^p)$ .

Numerical implementation of the modified Gurson–Tvergaard–Needleman model follows a similar procedure as outlined in Section 2.2.

### 3. Numerical examples

#### 3.1. Modeling the plastic behavior of an aluminum 5083 alloy

In this section we apply the  $I_1$ – $J_2$ – $J_3$  plasticity model to study the plastic response of an aluminum alloy 5083–H116, which was cold worked to achieve its strength. All specimens are machined from a 25 mm thick plate, with tensile axes oriented transversely to the rolling direction. Round specimens were turned with low stress machining procedures and rectangular specimens were electro-discharge machined. All tests are performed at room temperature and are considered to be quasi-static. The test matrix includes smooth and notched round tensile bars, grooved plane strain specimens and the Lindholm-type specimen (Lindholm et al., 1980) subjected to different tension–torsion ratios. Fig. 1 shows a smooth round bar, a notched round bar, a grooved plane strain specimen and a torsion specimen.

Two non-dimensional parameters defined as  $T = I_1 / (3\sqrt{3}J_2^{1/2})$  and  $\xi = 3\sqrt{3}J_3 / (2J_2^{3/2})$ , together with the equivalent stress  $\sigma_e$ , are often used to characterize the stress state, where  $T$  is the stress triaxiality ratio and  $\xi$  can be related to the Lode parameter (Wierzbicki and Xue, 2005; Xue, 2007; Kim et al., 2004, 2007; Gao et al., 2005, 2009, 2010). For the smooth and notched round tensile bars, the  $\xi$ -value at the center of the specimen is one while the  $T$ -value varies with the notch radius. The smaller the notch radius is, the higher the stress triaxiality. On the other hand, the  $\xi$ -value at the center of the grooved plane

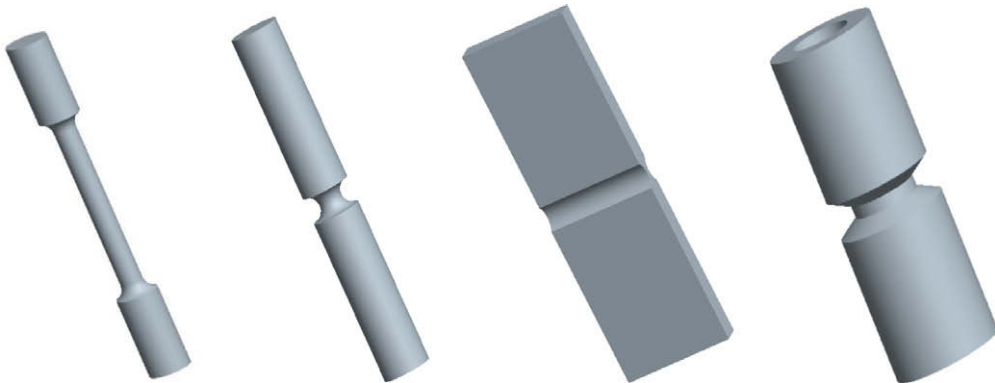


Fig. 1. Sketches of a smooth round bar, a notched round bar, a grooved plane strain specimen and a torsion specimen.



strain specimens is zero and the  $T$ -value varies with the groove radius. The Lindholm-type specimen can achieve various combinations of  $T$  and  $\xi$  by varying the ratio between the applied tensile displacement and the applied twist angle.

The diameter of the gage section of the smooth round bar is 6.35 mm. All the notched round bars have the same diameters of 15.2 mm in the smooth sections and 7.6 mm at their notched cross section. Three notch radii, 1.27, 2.54 and 6.35 mm, are considered for specimens D, B and E, respectively (Table 1). The overall dimensions for the circular-grooved plane strain specimens are  $203.2 \times 31.8 \times 6.1$  mm and the thinnest cross section is 2 mm. Three different groove radii, 2.03, 5.08 and 16.26 mm, are considered for specimens F, G and H, respectively (Table 2). The torsion specimens are hollow cylinders having an inner diameter of 13.1 mm and outer diameter of 23.8 mm. The gage section has a length of 2.54 mm and wall thickness of 0.75 mm. The torsion–tension specimens have a slightly larger outer diameter at both ends (25.4 mm) and other dimensions are the same as the torsion specimen. Table 3 lists the ratio between the applied tensile displacement and applied twist angle for each of the tension–torsion specimens. Details of specimen drawings are given in Gao et al. (2009).

The specimens in the test matrix of this study generate a wide range of stress states. Moreover, the stress-state of a material point in the test specimens evolves as plastic deformation increases. Figs. 2–5 show the variation of  $T = I_1 / (3\sqrt{3}J_2^{1/2})$  and  $\xi = 3\sqrt{3}J_3 / (2J_2^{3/2})$  with loading history (measured by the equivalent plastic strain,  $\bar{\epsilon}^p$ ) in the element at the specimen center for the smooth round bar, the E-notch round bar, the G-groove plane strain specimen and the TT-16 torsion–tension specimen. For the smooth round bar,  $\xi$  remains at 1 during the entire loading history while  $T$  increases from 1/3 to about 0.45 before specimen fractures. For the E-notch specimen,  $\xi$  remains at about 1 and  $T$  increases from 0.71 to 0.8. For the G-groove specimen,  $\xi$  quickly decreases to 0 and remains at this level as plastic deformation increases while  $T$  increases from 0.51 to 0.8 before failure occurs. For the tension–torsion specimen TT-16,  $\xi$  increases from 0.4 to 0.94 and  $T$  increases from 0.1 to 0.26. For the notched and grooved specimens, changing notch (groove) radius changes the level of  $T$  in the specimen. Considering the entire loading history of each specimen and the three different notch (groove) radii, the range of  $T$  experienced by the center element is  $0.71 \leq T \leq 1.6$  for the notched round bar tests and  $0.46 \leq T \leq 0.97$  for the plane strain tests. For the tension–torsion tests, varying the ratio between the applied tensile displacement and the applied twist angle results in different combinations of the  $\xi$  and  $T$  histories. Considering the entire loading history and the different tensile displacement/

**Table 1**

Notch radii of the notched round bars.

Specimen	B-notch	D-notch	E-notch
Notch radius (mm)	2.54	1.27	6.35

**Table 2**

Groove radii of the plane strain specimens.

Specimen	F-groove	G-groove	H-groove
Groove radius (mm)	2.03	5.08	16.26

**Table 3**

Ratios of the applied tensile displacement and applied twist angle used in the tension–torsion tests.

Specimen	TT-17	TT-19	TT-13	TT-16	TT-15	TT-14
tensile displacement/twist angle (mm/radian)	0.23	0.69	0.92	1.16	1.38	2.54

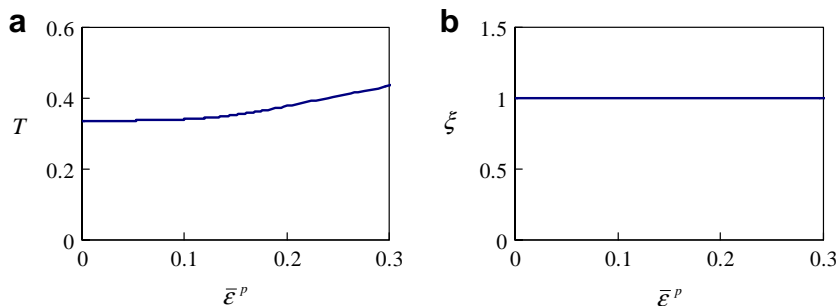


**Fig. 2.** Variation of  $T = I_1 / (3\sqrt{3}J_2^{1/2})$  and  $\xi = 3\sqrt{3}J_3 / (2J_2^{3/2})$  with plastic deformation in the center element of the smooth round bar.



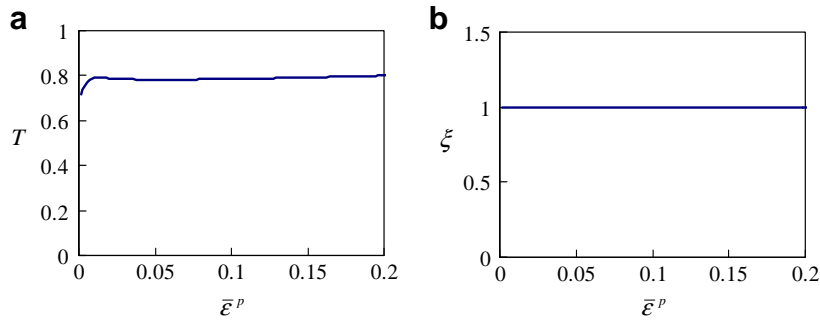


**Fig. 3.** Variation of  $T = I_1 / (3\sqrt{3}J_2^{1/2})$  and  $\xi = 3\sqrt{3}J_3 / (2J_2^{3/2})$  with plastic deformation in the center element of the E-notch specimen.

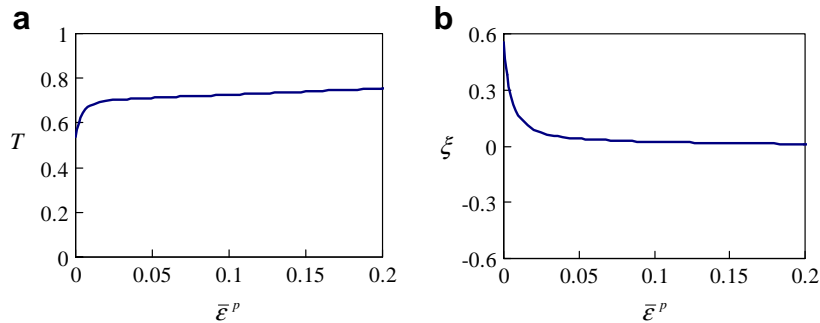


**Fig. 4.** Variation of  $T = I_1 / (3\sqrt{3}J_2^{1/2})$  and  $\xi = 3\sqrt{3}J_3 / (2J_2^{3/2})$  with plastic deformation in the center element of the G-groove specimen.

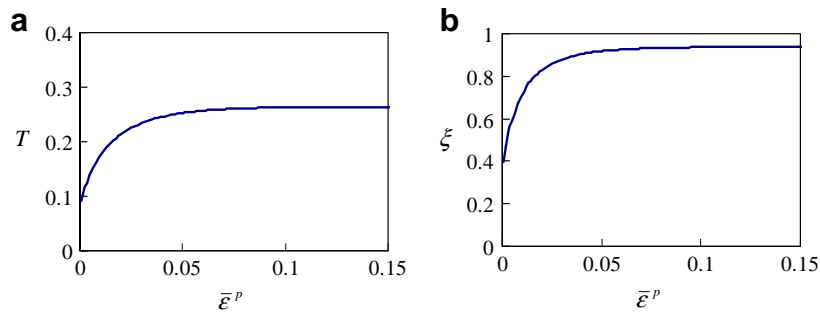


**Fig. 5.** Variation of  $T = I_1 / (3\sqrt{3}J_2^{1/2})$  and  $\xi = 3\sqrt{3}J_3 / (2J_2^{3/2})$  with plastic deformation in the center element of the tension–torsion specimen TT-16.

twist angle ratios listed in Table 3, the range of  $T$  and  $\xi$  experienced by the tension–torsion specimens in the test matrix are in the range of  $0.018 \leq T \leq 0.365$  and  $0.08 \leq \xi \leq 0.99$ .

Numerical analyses of the specimens are carried out using the general purpose finite element software ABAQUS (SIMULIA, 2008), which employs an updated Lagrangian formulation to handle finite deformation. The material models outlined in previous sections are implemented in ABAQUS via user defined subroutines. For round tensile bars, axisymmetric conditions are considered and the 4-node, axisymmetric solid elements with reduced integration (CAX4R) are used. For torsion–tension specimens, an additional degree of freedom needs to be added to the axisymmetric element to handle the twist and the CGAX4R element in ABAQUS is developed for this purpose. For grooved plane strain specimens, the 3D 8-node brick elements with reduced integration (C3D8R) are used. Usually the symmetry conditions allows for only 1/4 or 1/8 of the specimen being modeled. Fig. 6 shows two typical finite element meshes. A typical axisymmetric model has 700 elements and a typical 1/8-symmetric 3D model has 20,000 elements. Since reduced integration is used, the hourglass control is employed by using \*HOURLASS STIFFNESS in the ABAQUS input files to provide increased resistance to hourglassing.

Fig. 7 shows the true (von Mises) stress vs. plastic strain curves obtained using the smooth tensile bar data and the pure torsion test data. Gao et al. (2009) provides the details of how these two curves were obtained from the measured load–displacement and torque–twist angle curves, respectively. The two curves clearly show significant difference, suggesting that the stress-state has a strong effect on the plastic response of this material.

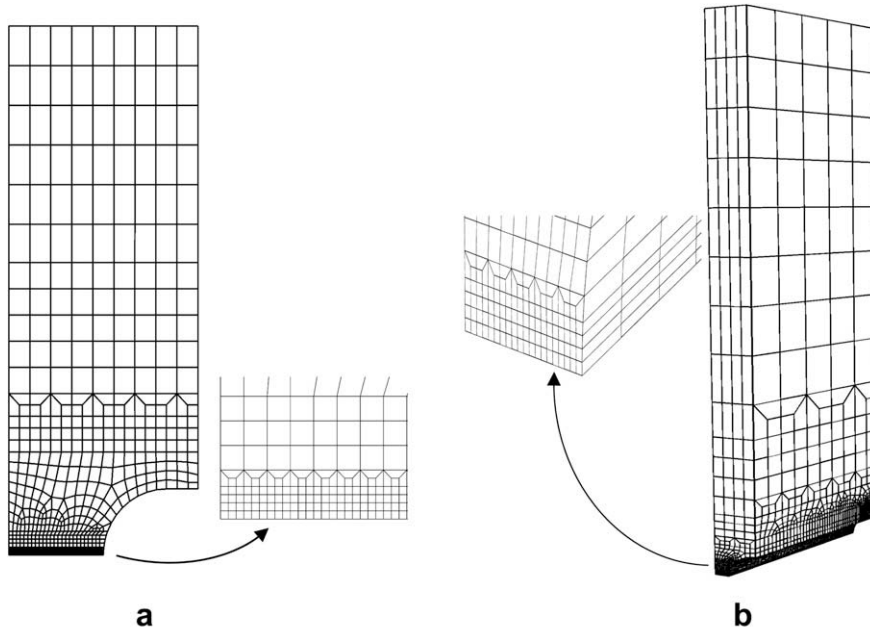


**Fig. 6.** Typical finite element meshes: (a) an axisymmetric model for a notched round bar, (b) a 1/8-symmetric model for a grooved plane strain specimen.

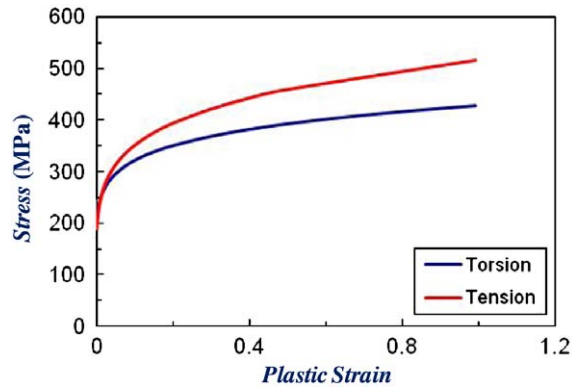


**Fig. 7.** Comparison of the true (von Mises) stress vs. true plastic strain curves obtained using the smooth tensile bar data and the torsion test data.

Now consider the  $I_1$ - $J_2$ - $J_3$  plasticity model presented in previous sections and conduct finite element analyses of these two specimens. The uniaxial tension stress–strain curve can be described by a power-law hardening relation

$$\begin{aligned} \varepsilon &= \frac{\sigma}{E} & \text{when } \sigma \leq \sigma_0 \\ \varepsilon &= \frac{\sigma_0}{E} \left( \frac{\sigma}{\sigma_0} \right)^{1/N} & \text{when } \sigma > \sigma_0 \end{aligned} \quad (37)$$

with  $E = 68.4$  GPa,  $\sigma_0 = 198.6$  MPa,  $\nu = 0.3$ , and  $N = 0.155$ . The plasticity model requires a relation of the current yield stress as a function of the effective plastic strain. This is achieved by using a UHARD subroutine. Using the uniaxial tension stress–strain curve and adjusting material parameters ( $a_1, b_1$ ) and ( $a_2, b_2$ ), it is found that a set of parameters,  $a_1 = a_2 = 0$ ,  $b_1 = -60.75$  and  $b_2 = -25$ , result in a best match between the numerically predicted and experimentally measured torque vs. twist angle response of the pure torsion test. This indicates no  $I_1$  effect but significant  $J_3$  effect on the plastic response. Fig. 8 compares the numerical predictions and the experimental measurements for the smooth tensile specimen and the pure torsion specimen, respectively. The tensile tests have seven specimens and the torsion tests have 10 specimens. The experimental data are represented by thinner lines while the finite element result is represented by a thicker line. In both cases, excellent comparison between the numerical prediction and the experimental measurements is observed.

With the parameters of the plasticity model being calibrated, the next question needs to be answered is whether this model correctly predicts the material response under complex stress states. To this end, notched round bars with different

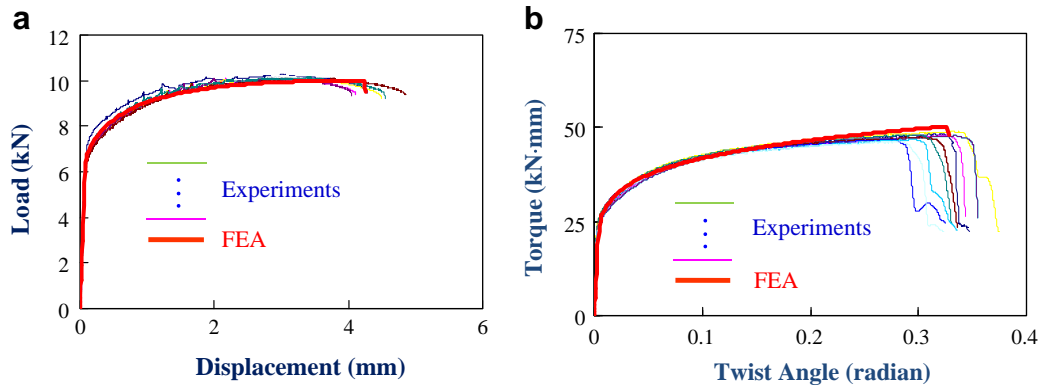


**Fig. 8.** Comparison of the numerical and experimental load vs. displacement curves for (a) the smooth tensile specimen and (b) the pure torsion specimen.

notch radii, plane strain specimens with different groove radii and torsion specimens subjected to different tension–torsion ratios are tested and analyzed and the numerical predictions are compared with the experimental records. For notched round bars and grooved plane strain specimens, the applied tensile force vs. extensometer gage displacement response is monitored. For tension–torsion specimens, both applied axial force vs. axial displacement and applied torque vs. twist angle responses are monitored. Fig. 9 shows typical comparisons – again, model predictions agree with experimental measurements very well. Similar comparisons between experimental results and numerical predictions are observed for all other specimens in the test matrix.

To further justify the proposed plasticity model, Fig. 10a and b compares the numerical predictions using the classical  $J_2$ -flow theory and the proposed  $I_1$ - $J_2$ - $J_3$  model for the tension–torsion test TT-16 with experimental results. In these figures, we also included the comparison between the non-associated flow rule (Non-AFR) and the associated flow rule (AFR). As can be seen from the plots, only the proposed  $I_1$ - $J_2$ - $J_3$  model with the calibrated parameters (non-associated flow rule) leads to good agreement with experimental records for both torque vs. twist angle and axial force vs. axial displacement. The asso-

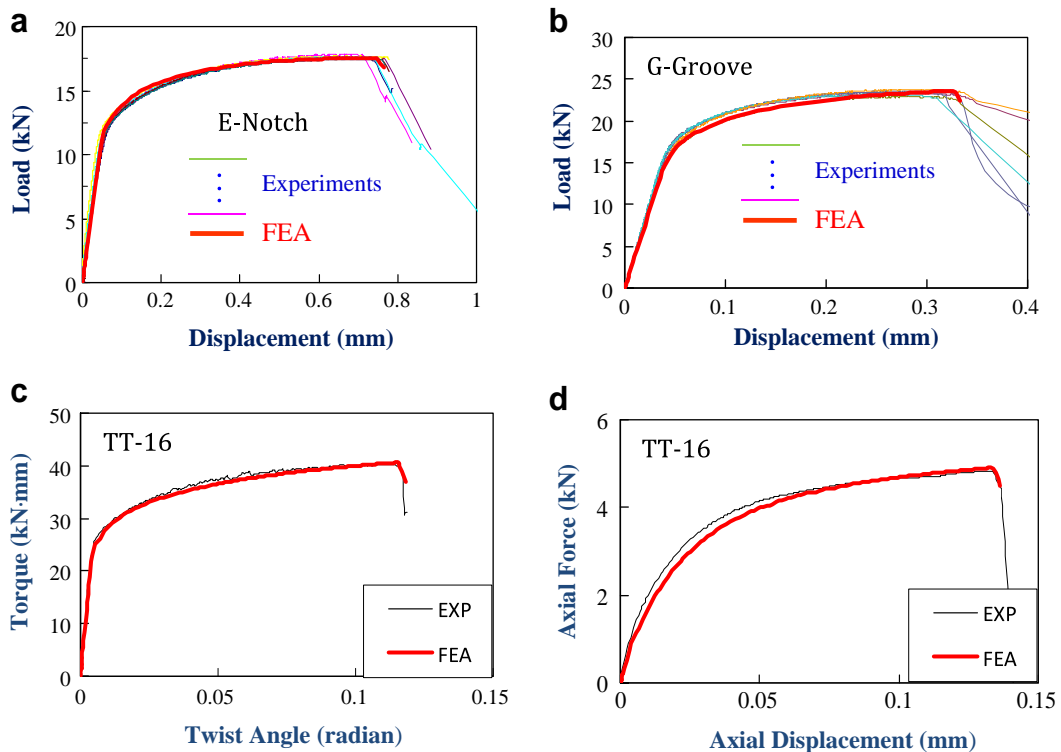


**Fig. 9.** Comparisons of the numerical predictions and experimental records: (a) notched round bar (E-Notch); (b) plane strain specimen (G-Groove); (c) torque vs. twist angle response for torsion–tension test (TT-16); (d) axial force vs. axial displacement response for torsion–tension test (TT-16).

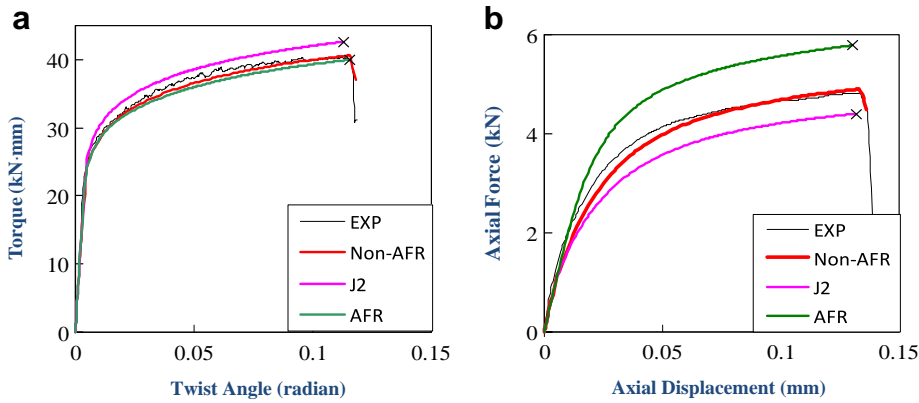


**Fig. 10.** Comparisons of the numerical predictions using the classical  $J_2$ -flow theory and the proposed  $I_1$ - $J_2$ - $J_3$  model for the tension–torsion test TT-16 with experimental results: (a) torque vs. twist angle; (b) axial force vs. axial displacement.

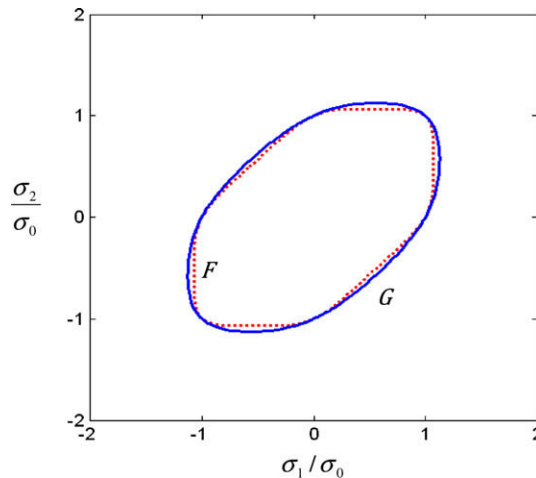
ciated flow rule gives acceptable torque vs. twist angle prediction but unsatisfying axial force vs. axial displacement prediction.

Fig. 11 shows the difference between the locus of the plastic flow potential ( $G$ ) and the locus of the yield function ( $F$ ) given by the  $I_1$ - $J_2$ - $J_3$  model with  $a_1 = a_2 = 0$ ,  $b_1 = -60.75$  and  $b_2 = -25$  on the  $\sigma_1$ - $\sigma_2$  plane, where the locus of the flow potential is represented by the solid line and the locus of yield function is represented by the dashed line.

In summary, the plasticity behavior of the 5083 aluminum alloy considered in this study depends on the stress state and can be described by an  $I_1$ - $J_2$ - $J_3$  plasticity model described in Section 2. The calibrated model constants are  $a_1 = a_2 = 0$ ,  $b_1 = -60.75$  and  $b_2 = -25$ , indicating no  $I_1$  effect but significant  $J_3$  effect on the plastic response of this material.

### 3.2. Numerical examples using the Gurson–Tvergaard–Needleman model

In this section we conduct a series of parametric studies to illustrate the effect of the modified Gurson–Tvergaard–Needleman model on predicted material response. Fig. 12 shows a cubic element with dimensions of  $D_0 \times D_0 \times D_0$ . Displacement boundary conditions are imposed on the element surfaces such that the macroscopic stress ratios,  $\rho_1 = \sigma_{11}/\sigma_{22}$  and  $\rho_2 = \sigma_{33}/\sigma_{22}$ , are kept constants during the entire deformation history (which results in a constant stress triaxiality ratio and Lode angle). Faleskog et al. (1998) and Kim et al. (2004) provide details of how to prescribe this kind of boundary conditions. The material parameters used in the analyses are  $E = 68.4$  GPa,  $\nu = 0.3$ ,  $\sigma_0 = 207$  MPa,  $N = 0.125$  and  $f_0 = 0.003$ , where  $E$ ,  $\nu$ ,  $\sigma_0$ ,  $n$  and  $f_0$  represent the Young's modulus, the Poisson's ratio, the yield stress, the strain hardening exponent and the initial void volume fraction, respectively. The  $q_1$  and  $q_2$  parameters in the Gurson–Tvergaard–Needleman model are taken as  $q_1 = 1.5$  and  $q_2 = 1$ .



**Fig. 11.** Comparison between the locus of the plastic flow potential ( $G$ ) and the locus of the yield function ( $F$ ) given by the  $I_1$ - $J_2$ - $J_3$  model with  $a_1 = a_2 = 0$ ,  $b_1 = -60.75$  and  $b_2 = -25$  on the  $\sigma_1$ - $\sigma_2$  plane.

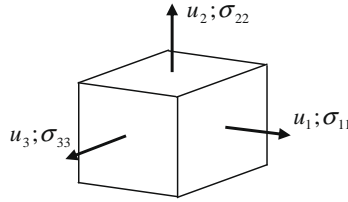


Fig. 12. A cubic element.

For the first set of analyses, the boundary conditions are imposed such that  $\rho_1 = 0.268$  and  $\rho_2 = 0.634$ , corresponding to a stress triaxiality ratio of 1 and Lode angle of  $0^\circ$ . When  $a_1 = a_2 = b_1 = b_2 = 0$ , the analysis results using our user subroutine are the same as those obtained using the original Gurson–Tvergaard–Needleman model implemented in ABAQUS, serving as a check of our numerical implementation.

Fig. 13 illustrates the effect of  $I_1$ , where the dotted lines represent the results obtained using  $a_1 = a_2 = b_1 = b_2 = 0$  and the solid lines represent the results obtained using  $a_1 = a_2 = 6 \times 10^{-4}$  and  $b_1 = b_2 = 0$ . At the same applied displacement in the  $x_2$ -direction ( $u_2$ ), both  $\sigma_{22}$  and the void growth rate are lower when the effect of  $I_1$  is taken into account.

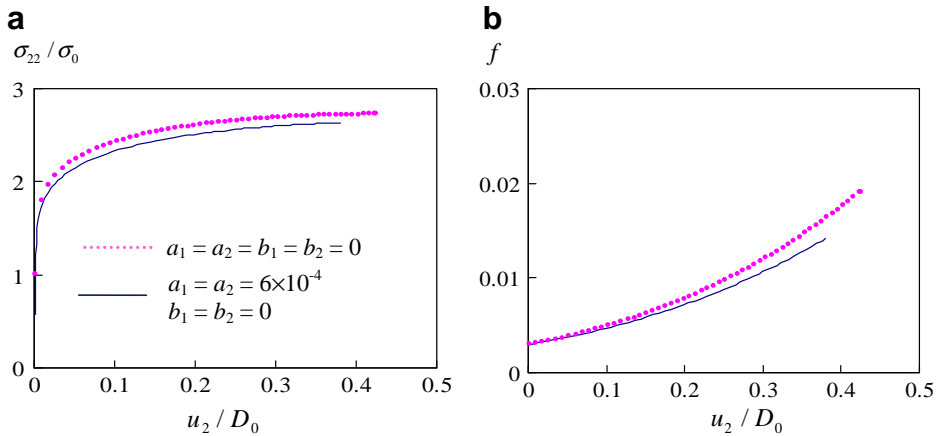


Fig. 13. Comparison of the  $\sigma_{22}/\sigma_0$  vs.  $u_2/D_0$  response and  $f$  vs.  $u_2/D_0$  response predicted using  $a_1 = a_2 = b_1 = b_2 = 0$  (dotted lines) and  $a_1 = a_2 = 6 \times 10^{-4}$  and  $b_1 = b_2 = 0$  (solid lines).

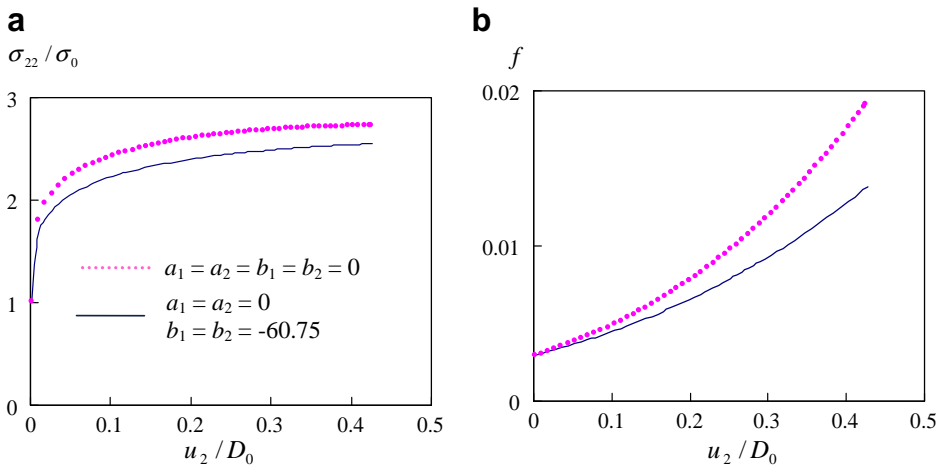
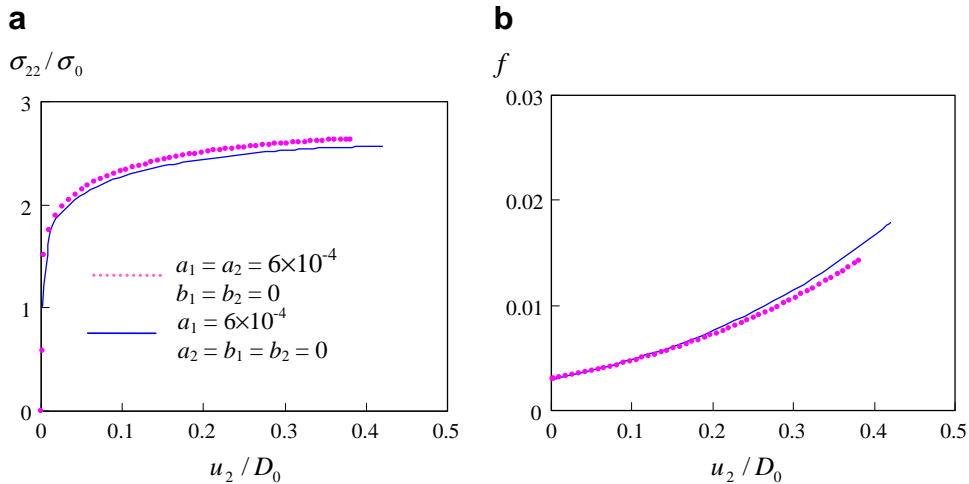


Fig. 14. Comparison of the  $\sigma_{22}/\sigma_0$  vs.  $u_2/D_0$  response and  $f$  vs.  $u_2/D_0$  response predicted using  $a_1 = a_2 = b_1 = b_2 = 0$  (dotted lines) and  $a_1 = a_2 = 0$  and  $b_1 = b_2 = -60.75$  (solid lines).



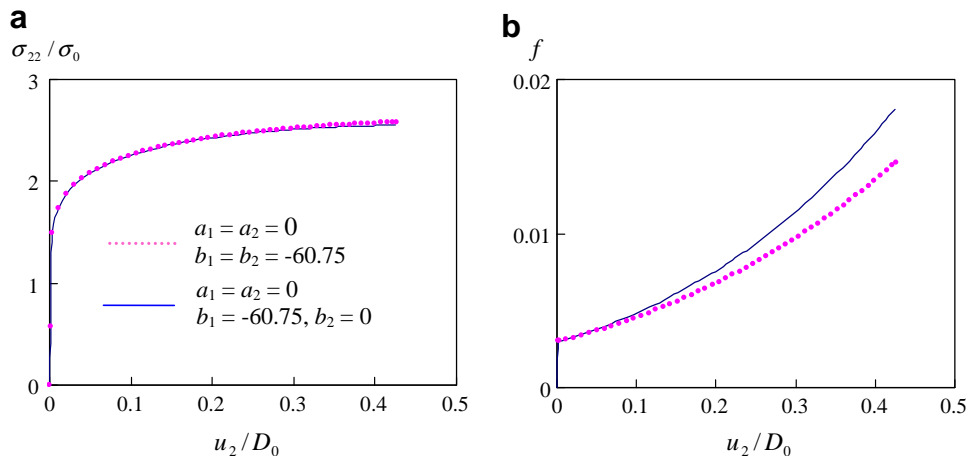
**Fig. 15.** Comparison of the  $\sigma_{22}/\sigma_0$  vs.  $u_2/D_0$  response and  $f$  vs.  $u_2/D_0$  response predicted using  $a_1 = a_2 = 6 \times 10^{-4}$  and  $b_1 = b_2 = 0$  (associated flow rule; dotted lines) and  $a_1 = 6 \times 10^{-4}$  and  $a_2 = b_1 = b_2 = 0$  (non-associated flow rule; solid lines).

Fig. 14 demonstrates the effect of  $J_3$  by setting non-zero values for  $b_1$  and  $b_2$ . Here the dotted lines show the results of  $a_1 = a_2 = b_1 = b_2 = 0$  and the solid lines are obtained by using  $a_1 = a_2 = 0$  and  $b_1 = b_2 = -60.75$ . The analysis results show that negative values of  $b_1$  and  $b_2$  lead to lower value of  $\sigma_{22}$  and slower void growth rate.

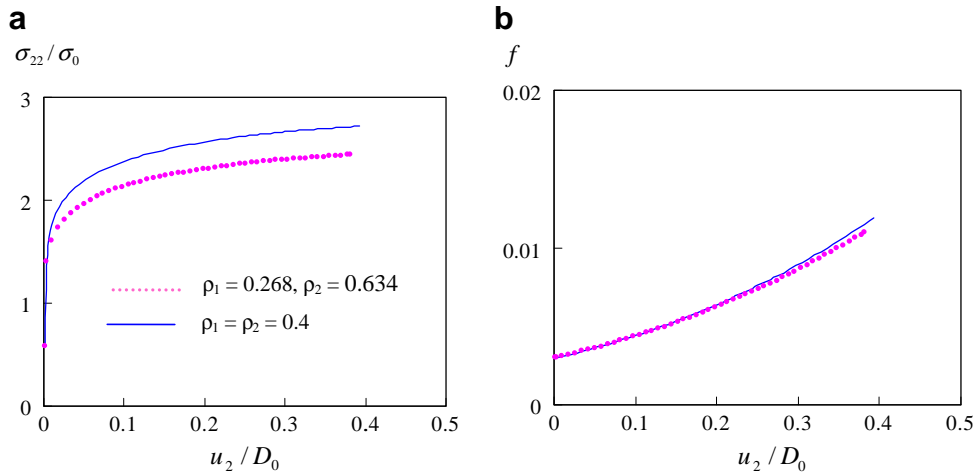
The results shown in Figs. 13 and 14 are obtained using the associated flow rule. Figs. 15 and 16 compare the results of the non-associated flow rule with those of the associated flow rule. As is shown in Fig. 15, where the dotted lines are the results of an associated flow rule ( $a_1 = a_2 = 6 \times 10^{-4}$  and  $b_1 = b_2 = 0$ ) and the solid lines are the results of a non-associated flow rule ( $a_1 = 6 \times 10^{-4}$  and  $a_2 = b_1 = b_2 = 0$ ), increasing  $a_2$  from 0 to  $6 \times 10^{-4}$  leads to an increase of  $\sigma_{22}$  and decrease of void growth rate.

Fig. 16 compares the results when  $b_2$  takes a different value than  $b_1$ . In these analyses,  $a_1$  and  $a_2$  are taken as zero and the results using  $b_1 = b_2 = -60.75$  (associated flow rule) are denoted by the dotted lines while the results using  $b_1 = -60.75$  and  $b_2 = 0$  (non-associated flow rule) are denoted by the solid lines. Varying  $b_2$  from 0 to  $-60.75$  results in negligible effect on  $\sigma_{22}$  but a higher void growth rate.

In the analyses presented above, the boundary conditions are imposed to keep  $\rho_1 = 0.268$  and  $\rho_2 = 0.634$ . The stress-state experienced by the material can be altered by changing the boundary conditions so that different values of  $\rho_1$  and  $\rho_2$  are achieved. For example,  $\rho_1 = 0.4$  and  $\rho_2 = 0.4$  corresponds to a stress triaxiality ratio of 1 and Lode angle of  $-30^\circ$ . Fig. 17 illustrates how this change of stress state (Lode angle changes from  $0^\circ$  to  $-30^\circ$  while stress triaxiality ratio remains 1) affects  $\sigma_{22}$  and the void growth rate, where  $a_1 = a_2 = 6 \times 10^{-4}$  and  $b_1 = b_2 = -60.75$  are used in the calculations. In Fig. 17, the dotted lines represent the results of  $\rho_1 = 0.268$  and  $\rho_2 = 0.634$  (Lode angle equal to  $0^\circ$ ) and the solid lines represent the results of



**Fig. 16.** Comparison of the  $\sigma_{22}/\sigma_0$  vs.  $u_2/D_0$  response and  $f$  vs.  $u_2/D_0$  response predicted using  $b_1 = b_2 = -60.75$  (dotted lines) and  $b_1 = -60.75$  and  $b_2 = 0$  (solid lines), where  $a_1$  and  $a_2$  are taken as zero.



**Fig. 17.** Comparison of the  $\sigma_{22}/\sigma_0$  vs.  $u_2/D_0$  response and  $f$  vs.  $u_2/D_0$  response when  $\rho_1 = 0.268$  and  $\rho_2 = 0.634$  (dotted lines) with those when  $\rho_1 = 0.4$  and  $\rho_2 = 0.4$  (solid lines), where  $a_1 = a_2 = 6 \times 10^{-4}$  and  $b_1 = b_2 = -60.75$ .

$\rho_1 = 0.4$  and  $\rho_2 = 0.4$  (Lode angle equal to  $-30^\circ$ ). The void growth rate is slightly higher and  $\sigma_{22}$  becomes noticeably larger when the Lode angle changes from  $0^\circ$  to  $-30^\circ$ .

In summary, the dependence of the matrix plasticity behavior on  $I_1$  and  $J_3$  results in significant changes in void growth and the macroscopic stress vs. deformation response of porous materials. The modified Gurson–Tvergaard–Needleman model provides a means to describe these changes.

#### 4. Concluding remarks

In this paper, we describe a plasticity model for isotropic materials, which is dependent on the second and third invariants of the stress deviator as well as the hydrostatic stress, and present its finite element implementation including integration of the constitutive equations using the backward Euler method and the formulation of the consistent tangent moduli. As an application, this model is calibrated and verified for a 5083 aluminum alloy. The model captures the strong stress-state effect on the plastic behavior of this material and accurately predicts the plastic responses of specimens experiencing a wide range of stress states. Furthermore, the Gurson–Tvergaard–Needleman porous plasticity model, which is widely used to simulate the void growth process of ductile fracture, is extended to include the effects of the third invariant of the stress deviator and the hydrostatic stress on the matrix material. A series of parametric studies illustrate the effects of model parameters on the predicted material response. This simple modification enriches the Gurson–Tvergaard–Needleman model and expands its applicability as a micromechanical model for ductile fracture.

#### Acknowledgements

This research is made possible by the funding from the Office of Naval Research N00014-09-1-0553 (Program Manager: Dr. Paul Hess).

#### References

- ABAQUS/Standard User's Manual (Version 6.9), 2008. SIMULIA, Providence, RI.
- Aravas, N., 1987. On the numerical integration of a class of pressure-dependent plasticity models. *Int. J. Numer. Meth. Eng.* 24, 1391–1416.
- Bai, Y., Wierzbicki, T., 2008. A new model of metal plasticity and fracture with pressure and Lode dependence. *Int. J. Plast.* 24, 1071–1096.
- Brunig, M., 1999. Numerical simulation of the large elastic–plastic deformation behavior of hydrostatic stress-sensitive solids. *Int. J. Plast.* 15, 1237–1264.
- Brunig, M., Berger, S., Obrecht, H., 2000. Numerical simulation of the localization behavior of hydrostatic-stress-sensitive metals. *Int. J. Mech. Sci.* 42, 2147–2166.
- Brunig, M., Chyra, O., Albrecht, D., Driemeier, L., Alves, M., 2008. A ductile damage criterion at various stress triaxialities. *Int. J. Plast.* 24, 1731–1755.
- Cazacu, O., Barlat, F., 2003. Application of representation theory to describe yielding of anisotropic aluminum alloys. *Int. J. Eng. Sci.* 41, 1367–1385.
- Cazacu, O., Plunkett, B., Barlat, F., 2006. Orthotropic yield criterion for hexagonal close packed metals. *Int. J. Plast.* 22, 1171–1194.
- Cazacu, O., Ionescu, I.R., Yoon, J.W., 2010. Orthotropic strain rate potential for the description of anisotropy in tension and compression of metals. *Int. J. Plast.* 26, 887–904.
- Cvitanic, V., Vlcek, F., Lozina, Z., 2008. A finite element formulation based on non-associated plasticity for sheet metal forming. *Int. J. Plast.* 24, 646–687.
- Drucker, D.C., 1949. Relations of experiments to mathematical theories of plasticity. *Trans. ASME J. Appl. Mech.* 16, 349–357.
- Drucker, D.C., Prager, W., 1952. Soil mechanics and plastic analysis of limit design. *Quart. Appl. Math.* 10, 157–165.
- Faleskog, J., Gao, X., Shih, C.F., 1998. Cell model for nonlinear fracture analysis-I. Micromechanics calibration. *Int. J. Fract.* 89, 355–373.
- Gao, X., Wang, T., Kim, J., 2005. On ductile fracture initiation toughness: effects of void volume fraction, void shape and void distribution. *Int. J. Solids Struct.* 42, 5097–5117.



- Gao, X., Zhang, T., Hayden, M., Roe, C., 2009. Effects of the stress state on plasticity and ductile failure of an aluminum 5083 alloy. *Int. J. Plast.* 25, 2366–2382.
- Gao, X., Zhang, G., Roe, C., 2010. A Study on the effect of the stress state on ductile fracture. *Int. J. Damage Mech.* 19, 75–94.
- Gurson, A.L., 1977. Continuum of ductile rupture by void nucleation and growth: part I—yield criteria and flow rules for porous ductile media. *J. Eng. Mater. Tech.* 99, 2–55.
- Hencky, H., 1924. Zur Theorie plastischer Deformationen und der hierdurch im Material hervorgerufenen Nachspannungen. *ZaMM* 4, 323–335.
- Hill, R., 1950. *The Mathematical Theory of Plasticity*. Oxford University Press, London.
- Hu, W., Wang, Z.R., 2005. Multiple-factor dependence of the yielding behavior to isotropic ductile materials. *Comput. Mat. Sci.* 32, 31–46.
- Kim, J., Gao, X., Srivatsan, T.S., 2004. Modeling of void growth in ductile solids: effects of stress triaxiality and initial porosity. *Eng. Fract. Mech.* 71, 379–400.
- Kim, J., Gao, X., 2005. A generalized approach to formulate the consistent tangent stiffness in plasticity with application to the GLD porous material model. *Int. J. Solids Struct.* 42, 103–122.
- Kim, J., Zhang, G., Gao, X., 2007. Modeling of ductile fracture: application of the mechanism-based concepts. *Int. J. Solids Struct.* 44, 1844–1862.
- Kuroda, M., 2004. A phenomenological plasticity model accounting for hydrostatic stress-sensitivity and vertex-type of effect. *Mech. Mater.* 36, 285–297.
- Levy, M., 1870. Mémoire sur les équations générales des mouvements intérieurs des corps ductiles au delà des limites en élasticité pourrait les ramener à leur premier état. *C. R. Acad. Sci.* 70, 1323–1325.
- Lindholm, U.S., Nagy, A., Johnson, G.R., Hoegfeldt, J.M., 1980. Large strain, high strain rate testing of copper. *J. Eng. Mater. Tech.* 102, 376–381.
- Ma, F., Kishimoto, K., 1998. On yielding and deformation of porous plastic materials. *Mech. Mater.* 30, 55–68.
- Mendelson, A., 1968. *Plasticity: Theory and Application*. Macmillan Publishing Company, New York.
- Mirone, G., Corallo, D., 2010. A local viewpoint for evaluating the influence of stress triaxiality and Lode angle on ductile failure and hardening. *Int. J. Plast.* 26, 348–371.
- Mroz, Z., 1963. Non-associated flow-laws in plasticity. *J. Méc. Théor. Appl.* 2, 21–42.
- Nemat-Nasser, S., Shokoh, A., 1980. On finite plastic flows of compressible materials with internal friction. *Int. J. Solids Struct.* 16, 495–514.
- Nemat-Nasser, S., 1983. On finite plastic flow of crystalline solids and geomaterials. *ASME J. Appl. Mech.* 50, 1114–1126.
- Nemat-Nasser, S., 1992. Phenomenological theories of elasto-plasticity and strain localization at high strain rates. *Appl. Mech. Rev.* 45, s19–s45.
- Plunkett, B., Cazacu, O., Barlat, F., 2008. Orthotropic yield criteria for description of the anisotropy in tension and compression of sheet metals. *Int. J. Plast.* 24, 847–866.
- Prandtl, L., 1925. Spannungsverteilung in plastischen Körpern. In: *Waltman Jr., J. (Ed.), Proceedings of the 1st International Congress on Applied Mechanics*. Delft, Technische Boekhandel en Drukkerij, pp. 43–54.
- Reuss, E., 1930. Berücksichtigung der elastischen Formänderungen in der Plastizitätstheorie. *Z. Angew. Math. Mech.* 10, 266–274.
- Runesson, K., Mroz, Z., 1989. A note on non-associated plastic flow rules. *Int. J. Plast.* 5, 639–658.
- Saint-Venant, B.de., 1870. Sur l'établissement des équations des mouvements intérieurs opérés dans les corps solides ductiles au-delà des limites où l'élasticité pourrait les ramener à leur premier état. *Comptes Rendus des Séances de* 70, 473–480.
- Simo, J.C., Taylor, R.L., 1985. Consistent tangent operators for rate-independent elasto-plasticity. *Comput. Methods Appl. Mech. Eng.* 48, 101–118.
- Soare, S., Yoon, J.W., Cazacu, O., Barlat, F., 2007. Applications of a recently proposed anisotropic yield function to sheet forming. In: *Banabic, D. (Ed.), Applications of a Recently Proposed Anisotropic Yield Function to Sheet Forming*. Springer, Berlin, Heidelberg, pp. 131–149.
- Spitzig, W.A., Sober, R.J., Richmond, O., 1975. Pressure dependence of yielding and associated volume expansion in tempered martensite. *Acta Metall.* 23, 885–893.
- Spitzig, W.A., Sober, R.J., Richmond, O., 1976. The effect of hydrostatic pressure on the deformation behavior of maraging and HY-80 steels and its implications for plasticity theory. *Metall. Trans.* 7A, 1703–1710.
- Stoughton, T.B., 2002. A non-associated flow rule for sheet metal forming. *Int. J. Plast.* 18, 687–714.
- Stoughton, T.B., Yoon, J.W., 2004. A pressure-sensitive yield criterion under a non-associated flow rule for sheet metal forming. *Int. J. Plast.* 20, 705–731.
- Stoughton, T.B., Yoon, J.W., 2006. Review of Drucker's postulate and the issue of plastic stability in metal forming. *Int. J. Plast.* 22, 391–433.
- Tresca, H., 1864. Memoir on the flow of solid bodies under strong pressure. *Comptes-rendus de l'académie des sciences* 59, 754.
- Tvergaard, V., 1981. Influence of voids on shear band instabilities under plane strain conditions. *Int. J. Fract.* 17, 389–407.
- Tvergaard, V., 1982. On Localization in ductile materials containing spherical voids. *Int. J. Fract.* 18, 237–252.
- Tvergaard, V., Needleman, A., 1984. Analysis of the cup–cone fracture in a round tensile bar. *Acta Metall.* 32, 157–169.
- von Mises, R., 1913. *Mechanik der festen Körpern im plastisch-deformablen Zustand*. Nachrichten von der königlichen Gesellschaft der Wissenschaften zu Göttingen. Mathematisch-Physikalische Klasse, 582–592.
- Wierzbicki, T., Xue, L., 2005. On the effect of the third invariant of the stress deviator on ductile fracture. Technical Report, Impact and Crashworthiness Lab, MIT.
- Xue, L., 2007. Damage accumulation and fracture initiation in uncracked ductile solids subject to triaxial loading. *Int. J. Solids Struct.* 44, 5163–5181.